# Structural and Electrochemical Evolution of Alloy Interfacial Layers in Anode-Free Solid-State Batteries

Stephanie Elizabeth Sandoval[1], John A. Lewis[1], Bairav S. Vishnugopi[2], Douglas Lars Nelson[1], Matthew M. Schneider[3], Francisco Javier Quintero Cortes[4], Christopher M. Matthews[5], John Watt[6], Mengkun Tian[7], Pavel Shevchenko[8], Partha P. Mukherjee[2], and Matthew T. McDowell[1,9*]

[1]School of Materials Science and Engineering, Georgia Institute of Technology, Atlanta, GA, 30332, USA
[2]School of Mechanical Engineering, Purdue University, West Lafayette, IN, 47907, USA
[3]Materials Science and Technology Division, Los Alamos National Laboratory, Los Alamos, NM 87545, USA
[4]Capacitor Foundry, LLC, Thousand Oaks, California, 91320, USA
[5]School of Electrical and Computer Engineering, Georgia Institute of Technology, Atlanta, GA, 30332, USA
[6]Center for Integrated Nanotechnologies, Los Alamos National Laboratory, Los Alamos, NM 87545, USA
[7]Institute for Electronics and Nanotechnology, Georgia Institute of Technology, Atlanta, GA, 30332, USA
[8]Advanced Photon Source, Argonne National Laboratory, Lemont, IL, 60439, USA
[9]George W. Woodruff School of Mechanical Engineering, Georgia Institute of Technology, Atlanta, GA, 30332, USA

*Corresponding author: mattmcdowell@gatech.edu

KEYWORDS

Solid-state batteries, anode-free batteries, lithium metal, alloy layers, interface dynamics, focused-ion beam, x-ray computed tomography, electrochemistry

*Lead contact

## SUMMARY

"Anode-free" solid-state batteries feature high energy density since there is no anode active material upon assembly. While beneficial effects of interfacial layers at the anode-solid electrolyte interface have previously been demonstrated, the mechanisms through which they influence lithium plating/stripping are unclear. Here, we reveal the evolution of 100-nm silver and gold interfacial layers during anode-free lithium plating/stripping using electrochemical methods, electron microscopy, synchrotron X-ray micro computed tomography, and modeling. The alloy layers significantly improve Coulombic efficiency and resistance to short circuiting, even though the alloys form solute regions or particulates that detach from the current collector as lithium grows. *In-situ* electrochemical impedance spectroscopy shows that the alloy layers return to the interface and mitigate contact loss at the end of stripping, avoiding a critical vulnerability of anode-free cells. The enhanced contact retention is driven by uniform Li thickness that promotes spatially uniform stripping, as well as local alloy delithiation in response to current concentrations to homogenize current and diminish voiding.

## INTRODUCTION

Solid state batteries (SSBs) are a promising next-generation energy storage technology which could enable the reliable use of lithium (Li) metal anodes, thus providing higher energy density than Li-ion batteries.[1–6] "Anode-free" SSBs, which feature a lithiated cathode (such as $LiNi_xCo_yMn_zO_2$) paired with a current collector without active material present, are of particular interest due to their minimal volume and high energy density.[7–16] The first charge of anode-free SSBs involves the *in situ* growth of Li metal on the current collector, which simplifies manufacturing since Li metal does not need to be directly incorporated.[12,15]

Conventional SSBs with excess Li metal face fundamental issues associated with dynamics at the Li/solid-state electrolyte (SSE) interface.[7,17–20] Contact loss occurs when Li is stripped from the interface too rapidly to be replenished by self-diffusion or mechanical deformation,[21–25] and this causes current concentrations and growth of Li filaments on subsequent plating steps.[25–28] Anode-free SSBs feature additional challenges that arise due to the chemical/structural mismatch between Li and the current collector.[10,15] The nature of the interaction between Li and the current collector during initial electrodeposition will affect the nucleation behavior of Li and its subsequent morphological evolution throughout cycling. It is also critical that all the Li can be accessed during stripping to achieve high Coulombic efficiency (CE) since there is no excess Li present.

While there has been a large body of work focused on understanding Li deposition/stripping behavior in Li-excess metal batteries using both solid and liquid electrolytes,[17,26,29–32] there has been minimal focus on understanding Li behavior in anode-free SSBs. This is important since the growth of Li directly on a current collector could be governed by different mechanisms than Li-excess cells. Recent work has investigated anode-free Li growth

using current collectors hot-pressed on $Li_7La_3Zr_2O_{12}$ (LLZO) SSEs, where the influences of stack pressure and adhesion forces were examined.[9,33] It has also been found that the thickness of Li affects plating/stripping mechanisms.[34] Our recent work has revealed that localized Li depletion and island formation near the end of stripping play a critical role in limiting the performance of anode-free SSBs.[35] During stripping from anode-free cells with argyrodite SSEs, slightly non-uniform Li thicknesses led to some Li regions being fully stripped before others, locally exposing the electrochemically-inactive current collector and leading to current constriction, void growth, and rapid short circuiting upon cycling. This mechanism is unique to anode-free cells since it only occurs when attempting to strip all Li, and it significantly reduces cell stability compared to Li-excess cells. Thus, strategies are needed to improve growth/stripping uniformity and to simultaneously mitigate the formation of isolated islands and current concentration as the last Li is stripped.

Interfacial materials, including Li alloys and others, have previously been investigated in anode-free and Li-excess SSBs to improve cycling.[36–41] Silver-carbon composite layers can facilitate uniform cyclic Li deposition/stripping.[12] Telluride layers have also been shown to promote uniform growth.[38] Lithium-magnesium alloy interfaces can enhance diffusion and diminish voiding.[42] While these studies have shown improved cell performance, there is a lack of knowledge of the mechanistic influence of interfacial layers on the evolution of Li in anode-free SSBs.

Here, we investigate the structural and electrochemical evolution of silver (Ag) and gold (Au) alloy interlayers in sulfide ($Li_6PS_5Cl$) anode-free SSBs, finding that these materials enable uniform Li growth/stripping and act to mitigate contact loss at the end of stripping through responsive current homogenization. Both alloy layers enhance cycling stability and CE compared

to bare copper (Cu). The alloy layers allow for uniform Li nucleation and growth, as revealed by synchrotron X-ray micro computed tomography (μCT), and cryo/plasma-focused ion beam (FIB) shows that the alloy layers break into particles and disperse throughout the Li layer during Li growth. *In situ* electrochemical impedance spectroscopy (EIS) reveals that bare Cu exhibits contact loss signatures at the end of stripping, but that both alloy layers return to the interface to maintain interfacial contact to improve cycling stability despite significant morphological evolution. The improved contact retention and stability are enabled by the spatially uniform growth of Li, as well as the proposed ability of these alloys to locally de-alloy to release Li and prevent current concentrations at the end of stripping, as supported by mesoscale modeling. These results provide critical new mechanistic insight into the dynamics of anode-free interfacial layers that should help guide SSB engineering.

## RESULTS AND DISCUSSION

### Electrochemistry of Alloy Interlayers

We first investigated the influence of alloy interlayers on electrochemical cycling of anode-free half cells. Half cells were fabricated with the $Li_6PS_5Cl$ (LPSC) SSE, Li metal counter electrodes, and 10-μm thick Cu foil working electrodes. For cells with alloy layers, 100-nm Ag or Au films were evaporated onto the Cu before cell assembly (Fig. S1). Cells were cycled with a current density of 0.25 mA $cm^{-2}$ and areal capacity of 1.0 mAh $cm^{-2}$ with a stack pressure of 15 MPa (see Experimental Procedures). Figure 1a shows typical voltage curves for bare Cu, Ag-coated, and Au-coated electrodes over six cycles. The Cu cell short circuited in the fifth deposition half-cycle (arrow in Fig. 1a); the Cu cells consistently short circuited within the first five cycles with eight cells tested. In contrast, the cells with alloy-modified electrodes typically sustained up

to 30 cycles without short circuiting. The overpotential during deposition on the bare Cu electrode was the highest of all three cells, slightly increasing from ~11 mV in the first cycle to ~15 mV in the fifth cycle, whereas the alloy-modified electrodes exhibit ~8-10 mV deposition voltages.

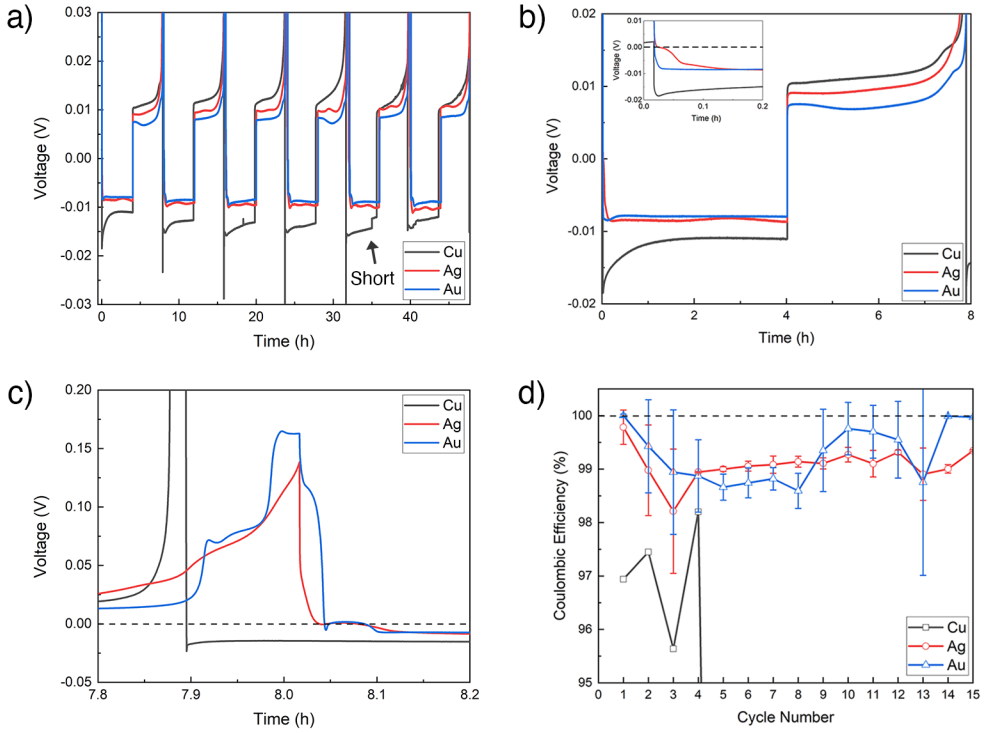


**Figure 1. Electrochemistry of alloy-modified Cu foils in anode-free half cells.** (a) Voltage curves during galvanostatic plating/stripping of Li in half cells onto bare Cu foil, Cu with 100 nm of Ag, and Cu with 100 nm of Au. A current density of 0.25 mA $cm^{-2}$ and an areal capacity of 1.0 mAh $cm^{-2}$ were used. (b) Magnified view of the first cycle from (a), with the inset showing the first 12 min of deposition. (c) Magnified view of the end of the first stripping step from (a). (d) Average CEs with cycling for half cells with bare Cu and alloy-modified Cu electrodes. The Au and Ag datasets are the average of four cells, while the Cu is from a single cell.

Figure 1b shows a magnified view of the first cycle, with the inset highlighting the first 12 min of deposition. The cell with bare Cu exhibits a nucleation overpotential of ~18 mV, while the Ag- and Au-coated electrodes have minimal nucleation overpotential, as has previously been observed for Cu[43–45] and alloy-modified interfaces[22,46] in liquid cells. The lack of obvious nucleation overpotential for the Ag- and Au-modified electrodes is due to alloying of the interfacial

layers, which is known to provide for preferential nucleation of Li metal.[46] The inset in Fig. 1b shows that the Ag-coated electrode has an alloying plateau around 0 V, while the Au-coated electrode does not exhibit its expected plateau at 80 mV perhaps due to initial kinetics limitations. Clear signatures of Au dealloying are visible at the end of the first cycle, however (Fig. 1c), indicating that alloying of Au does occur during the first cycle.

The three types of cells also show divergent behavior at the end of the stripping step, as shown in the magnified view in Fig. 1c. The stripping process of the bare Cu electrode ends earlier (at ~7.9 h) than the other two, signifying lower CE and more stranded Li. The bare Cu cell also shows a sharp voltage increase at the end of stripping due to exhaustion of available Li, potentially correlating to current constrictions/void growth at remaining Li islands.[35] In contrast, the Ag-modified cell shows a sloping potential trace from 7.8 h due to extraction of Li from the Li-Ag alloy. The Au-modified cell shows two plateaus at ~70 mV and ~160 mV corresponding to Li-Au delithiation. Alloy delithiation occurs after Li metal stripping since the delithiation potentials are higher than that for Li metal stripping. At the beginning of the second deposition (Fig. 1c), both the Ag and Au layers show lithiation plateaus, and thus the interlayers continually undergo alloying and dealloying during cycling. Based on the thickness of the metal films, we expect a theoretical areal capacity of 78 μAh $cm^{-2}$ for Au and 26 μAh $cm^{-2}$ for Ag, which is consistent with the data in Fig. 1a-c.

Figure 1d shows the average CE during cycling of half cells with Ag- and Au-coated electrodes (four cells averaged for each). These are compared to the CE values from one bare-Cu cell, which short circuits in the fifth cycle and shows very low CE values (Fig. S2). The alloy-modified electrodes display high initial average CEs of 99.78% (Ag) and 99.98% (Au), while that for bare Cu is 96.94%. Over the first ten cycles, the Ag cells yield an average CE of 99.06% and

the Au cells yield 99.12%. Despite their similar CEs, Ag-coated cells usually short circuited around cycle 30 while the Au-coated electrodes short circuited around cycle 15. Anode-free full cells with NMC cathodes also showed similar improvements in stability and CE when Ag and Au layers were used (Fig. S3).

**Structural and Morphological Evolution during Cycling**

To investigate the structure of the deposited Li, focused ion beam (FIB) milling coupled with scanning electron microscopy (SEM) imaging were employed. Both plasma FIB (PFIB) and cryogenic $Ga^+$ FIB (cryo-FIB) were used to minimize beam damage and material redeposition.[47–50] Figure S4 highlights the advantages of cryo-FIB; milling at -145 °C with a $Ga^+$ beam maintains dense Li, while milling at 25 °C destroys the morphology of the sample. Plasma FIB does not require cryogenic temperatures because of minimal interaction between the $Xe^+$ plasma beam and Li. Half cell stacks were extracted from the cell housings after Li deposition, and milling was then performed through the 10-μm thick Cu current collector, the electrodeposited Li, and into the SSE, as shown in Fig. S5.

Figure 2a-c shows SEM images and X-ray energy dispersive spectroscopy (EDS) maps of 1.0 mAh $cm^{-2}$ of deposited Li after PFIB milling, which corresponds to a theoretical Li thickness of 5 μm. The Li electrodeposited on bare Cu (Fig. 2a) is non-uniform and well below its expected thickness (~3.4 μm at its thickest point). Thickness variations across the electrode have previously been observed when using bare Cu in anode-free cells.[35] There are regions of porosity within the Li layer, and the Li also clearly grows into pores of the SSE. EDS shows Cu and sulfur signatures on either side of the Li layer, verifying the chemical nature of these layers.

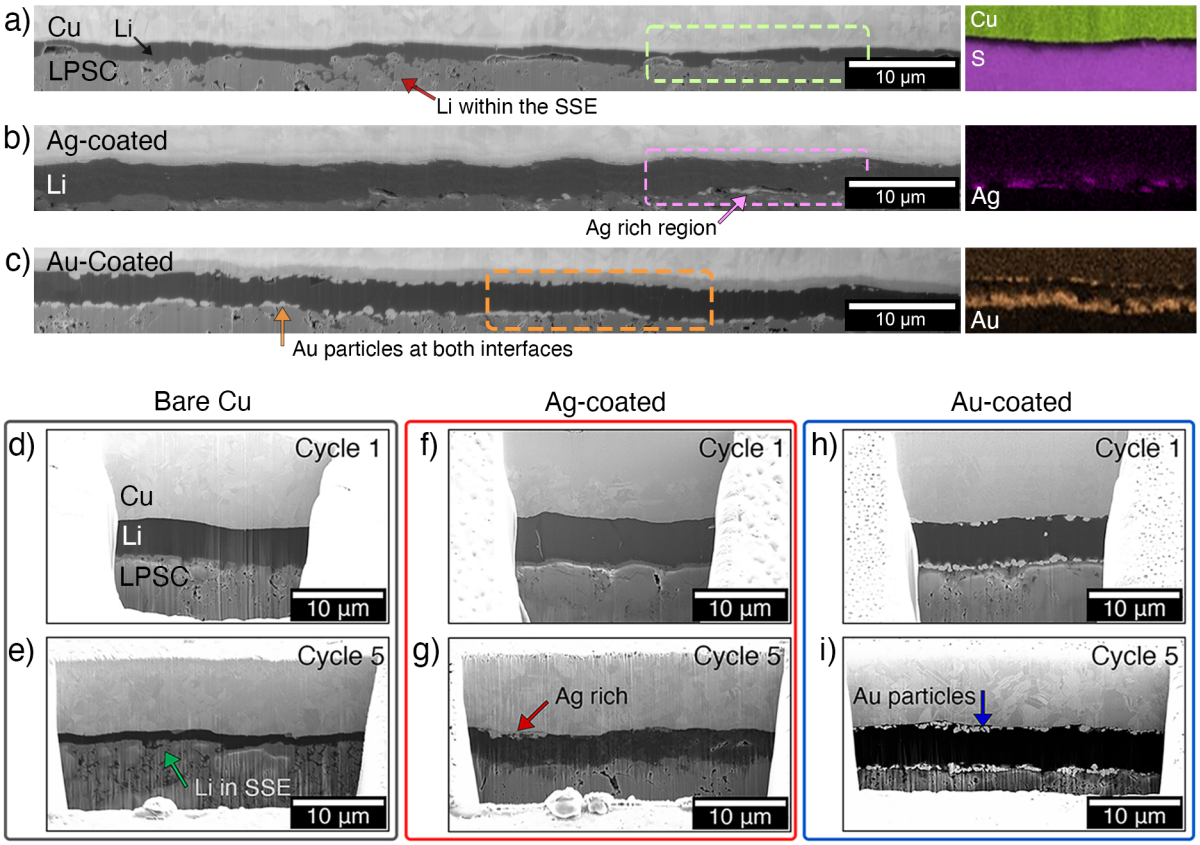


**Figure 2. Cross-sectional PFIB and cryo-FIB-SEM characterization at different stages of cycling.** 1.0 mAh $cm^{-2}$ of Li was deposited per half cycle at a current density of 0.25 mA $cm^{-2}$ onto the various electrodes. (a) PFIB-SEM image of deposited Li on a bare Cu electrode. (b) PFIB-SEM image of deposited Li on an Ag-coated Cu electrode, in which Ag particles are visible. (c) PFIB-SEM image of deposited Li on an Au-coated Cu electrode, in which Au particles are visible on the top and bottom of the Li. EDS spectra of local regions (as indicated by the dotted rectangles) are shown next to each image in (a-c). (d-e) Cryo-FIB-SEM images of Li deposited onto bare Cu electrodes after the (d) first and (e) fifth deposition cycles. (f-g) Cryo-FIB-SEM images of Li deposited onto Ag-modified Cu electrodes after the (f) first and (g) fifth deposition cycles. (h-i) Cryo-FIB-SEM images of Li deposited onto Au-modified Cu electrodes after the (h) first and (i) fifth deposition cycles.

Li grows much more uniformly on the alloy-coated electrodes (Fig. 2b-c), with thicknesses closer to the expected theoretical value for both (~5.3 µm and ~5.1 µm at the thickest points for Ag- and Au-coated electrodes, respectively). The-alloy modified cells also do not exhibit obvious Li growth within the SSE pores, which likely arises from the more uniform nucleation enabled by the alloys. For both alloy interlayers, the expected thickness of Li should be similar to the pure Li

case since the same areal capacity of Li is deposited and the (partial) molar volumes of Li in the alloy and pure Li are similar.[23,51] On the Ag-coated electrode (Fig. 2b), bright Ag-rich particles are scattered nonuniformly throughout the Li layer, with some near the Li||LPSC interface, as confirmed with EDS. Since Ag and Li form a solid solution,[46,52–54] we also expect that Ag is dissolved throughout the Li layer at concentrations too low for reliable EDS detection. On the Au-coated electrode (Fig. 2c), bright-contrast Au particles are visible both at the Cu-Li and Li-SSE interfaces. Upon lithiation, the initially dense Au film breaks up into Li-Au particles, with about half remaining at the Cu-Li interface and half attached to the Li-SSE interface, separated by the expanding Li metal. This interesting phenomenon may be due to bonding between Au and sulfur in the LPSC, or it may be driven by other factors.

To characterize the evolution of interfacial morphology with cycling, cryo-FIB/SEM was conducted after the first, second, and fifth deposition half-cycles with 1.0 mAh $cm^{-2}$ of Li deposited each cycle (Fig. 2d-i, Fig. S6). After the first deposition, the bare Cu electrode (Fig. 2d) shows a slightly thinner Li layer than the expected theoretical thickness of 5.0 μm. After the second deposition (Fig. S6a), the bare Cu has slightly greater thickness than theoretically expected, indicating nonuniform growth across the electrode. After the fifth cycle on bare Cu (Fig. 2e), the Li is thin and nonuniform, with significant Li growth observed within the SSE (this cell short-circuited before the fifth cycle).

Figure 2f-g shows Li deposited onto Ag-modified electrodes over five cycles. After initial deposition (Fig. 2f), the Li layer is of uniform ~5.0 μm thickness. Thin slivers of lighter-contrast Ag are visible within the Li. After the second cycle (Fig. S6b), there are no obvious changes in the structure or morphology. After the fifth cycle, however, there is some agglomeration of Ag at the Cu-Li interface (Fig. 2g, red arrow). This agglomeration may result in performance degradation

with cycling. Figure 2h-i shows Li deposited onto Au-modified electrodes. After the first deposition (Fig. 2h), the Au particles are observed on either side of the uniform, ~5.2 μm Li layer, as in the PFIB data in Fig. 2c. The morphology after the second cycle (Fig. S6c) is similar, but after five cycles the Au particles appear to show some particle agglomeration at the top and bottom of the Li layer (Fig. 2i). Comparing these cases, the solubility of Ag in Li[53] likely results in most of the Ag being dissolved in the Li layer since there are minimal particulates observed. The insolubility of Au in Li[55] causes Li-Au alloy particles to be present. Despite these different mechanisms, both materials act to substantially enhance Li uniformity and CE in these anode-free cells.

While FIB characterization enables effective imaging of buried interfaces, it is limited to relatively small, localized regions. To understand the influence of alloy layers across entire interfaces, synchrotron X-ray μCT was leveraged (see Experimental Procedures). Figure 3a-b shows reconstructed image slices of half cells after 2 mAh $cm^{-2}$ of Li was deposited onto (a) bare Cu and (b) Ag-coated electrodes using a current density of 0.5 mA $cm^{-2}$. Magnified views of the working electrode interfaces (red box) are shown below the reconstructed images. On the bare Cu electrode (Fig. 3a), the Li grows nonuniformly in this two-dimensional slice, with thickness variations and growth into cracks near the interface. The lithium growth on the Ag-coated electrode (Fig. 3b) is much more uniform, consistent with the FIB data.

Image segmentation was carried out to extract the position of the Li regions and the SSE, and Figure 3c-d show three dimensional renderings of the Li and SSE phases from a subvolume with 0.65 mm edge length in the center of the cells. In the cell with bare Cu (Fig. 3c), the Li distribution within this volume is highly nonuniform, with inconsistent coverage across the interface and lithium growth within cracks within the SSE (as is evident from the 2D view in Fig.

3a). In the cell with Ag-coated Cu (Fig. 3d), the Li features much more uniform thickness over this subvolume, with no Li growth observed within the SSE. For additional quantification, Figure 3e-f show Li thickness maps for these two subvolumes. These thickness maps show the total Li thickness at each position at the interface regardless of whether the Li is at the current collector or has grown within the SSE. The bare Cu cell features variable Li thickness that ranges from zero to ~40 µm across the interface with an average thickness of 6.7 µm (Fig. 3e), whereas the Ag-coated Cu cell exhibits much more uniform thickness with an average thickness of 10 µm (Fig. 3f). Overall, these volumetric data are consistent with the FIB data in Fig. 2, demonstrating that the Ag layer enables uniform growth of Li across the SSE interface.

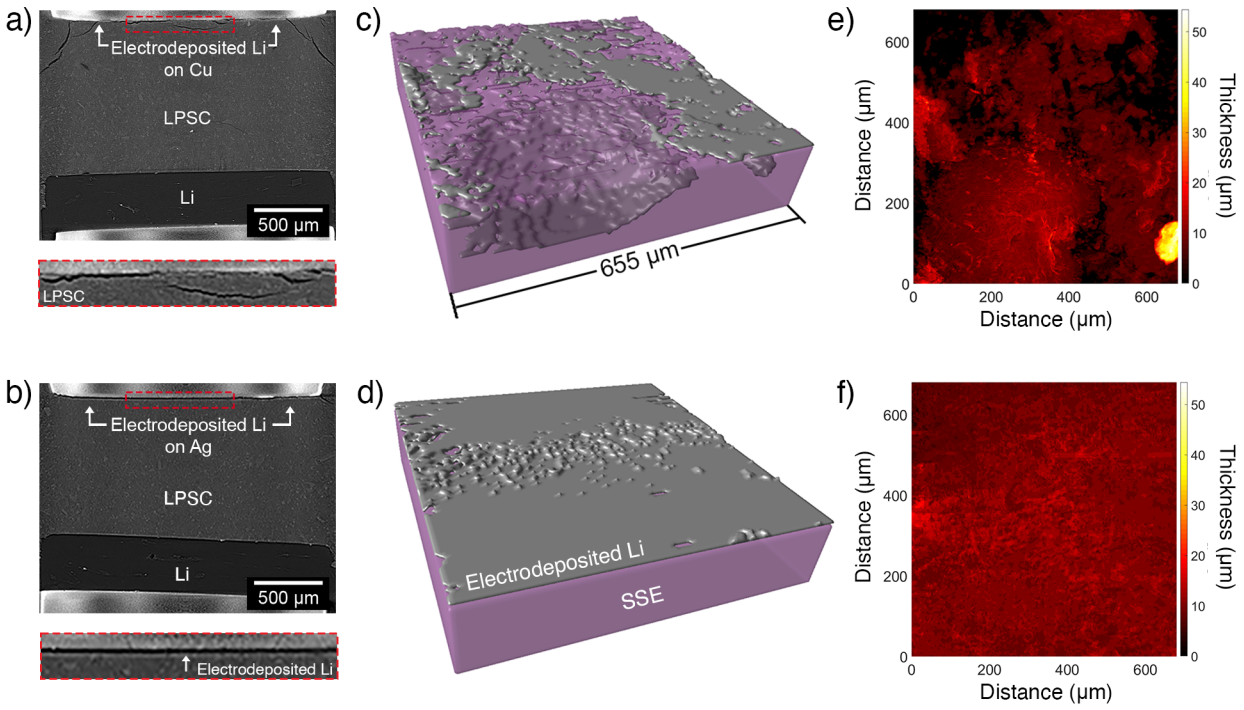


**Figure 3. Synchrotron X-ray micro computed tomography characterization of bare Cu and Ag-coated electrodes after electrodeposition.** (a-b) Reconstructed image slice taken from a scan of anode-free half cells with (a) bare Cu and (b) Ag-coated electrodes after deposition of 2 mAh $cm^{-2}$ of Li using a current density of 0.5 mA $cm^{-2}$. Magnified views of the interface are included below each image. (c-d) 3D renderings of a subvolume at the Li/LPSC interface for the cells with (c) bare Cu and (d) Ag-coated electrodes. The SSE is shown in purple and the electrodeposited Li is gray. The subvolume locations are highlighted by the red rectangles in (a-b). (e-f) Thickness

maps showing the Li thickness across the (e) bare Cu and (f) Ag-coated interfaces from the subvolumes in (c-d). The thickness maps are generated by summing the entire Li thickness at each pixel, regardless of whether the Li is at the current collector or within cracks in the SSE.

**Correlation to Interfacial Impedance Evolution**

To further probe the influence of alloy layers on interfacial evolution, Fig. 4a shows potentiostatic EIS data collected in the initial state and after each of the first five stripping cycles for the electrodes. These data are fitted with an equivalent circuit model consisting of a parallel resistor/constant phase element (CPE) combination in series with a resistor and Warburg element (see inset in Fig. 4b). The top panel of Fig. 4a shows data from a bare Cu electrode. In the pristine state before Li deposition, the spectrum contains a semicircle with a Warburg tail at lower frequencies, indicating blocking behavior. The semicircles grow after each successive cycle. The semicircles correspond to interfacial impedance of the working electrode, and the high frequency intercept with the *x*-axis is the approximate bulk electrolyte resistance.[56,57] Furthermore, since symmetric Li/Li cells showed negligible interfacial impedance (<1 Ω $cm^2$) and minimal spectral changes with cycling (Fig. S7), this verified that the Li/SSE interface at the counter electrode in Fig. 4a does not contribute to impedance changes under these cycling conditions, and that any interphase that forms does not alter the spectra over the time period tested. Previous work has also shown minimal changes of the interfacial resistance with time in symmetric cells held at open circuit[58]. Thus, the increasing semicircle width in Fig. 4a corresponds to increasing interfacial impedance of the Cu working electrode, as shown by the extracted $R_2$ values that increase from 3.5 to 27 Ω $cm^2$ over the five cycles (Fig. 4b).

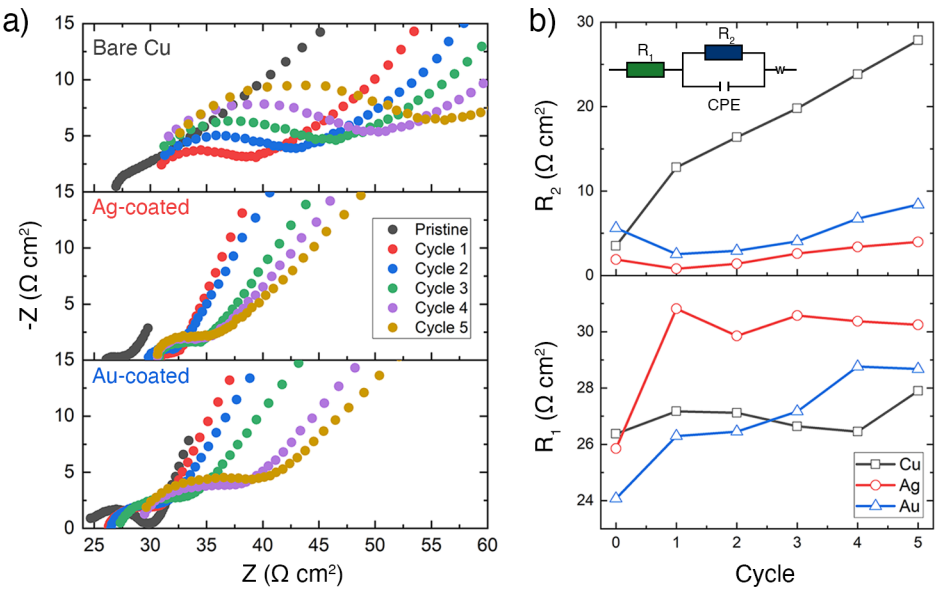


**Figure 4. EIS spectra with cycling.** Spectra were collected in the pristine state and after each of the first five cycles for (a) bare Cu (top), Ag-coated (middle), and Au-coated (bottom) electrodes in half cells. Cells were cycled at 0.25 mA $cm^{-2}$ with an areal capacity of 1.0 mAh $cm^{-2}$ per cycle. (b) Extracted resistance values from the spectra in (a) fit with the equivalent circuit shown in the inset. The series resistance ($R_1$) and interfacial resistance ($R_2$) are plotted in the pristine state (cycle 0) and over the first five cycles. Given the lack of access to higher-frequency information, the series resistance $R_1$ is assumed to stretch from the intercept of the $R_2$ semicircle to the origin.

The Ag-modified electrode (Fig. 4a, middle panel) exhibits more stable EIS spectra over these cycles. The spectrum from the pristine electrode shows a small semicircle signifying minimal interfacial impedance, along with a Warburg tail. The spectra shift to the right after the first cycle, corresponding to an increase of the $R_1$ value in Fig. 4b; this is likely due to increased apparent bulk SSE resistance caused by rearrangement of the Ag at the interface inducing different current pathways.[59] There are also minor increases of the interfacial resistance $R_2$ with cycling (less than 1 Ω $cm^2$ each cycle), as shown in Fig. 4b. The Au-modified electrode (Fig. 4a, bottom panel) shows similar behavior with minor increases in interfacial resistance with cycling, albeit with slightly larger initial interfacial resistance. Taken together, these impedance spectra show that both

the Ag- and Au-modified electrodes exhibit lower and more stable interfacial resistance compared to the bare Cu electrode.

Further *in situ* potentiostatic EIS experiments were undertaken to track spectral evolution at 10-min intervals over the course of individual half cycles (see Experimental Procedures). The results reveal divergent behavior among the three types of electrodes, which corresponds directly to interface morphology evolution. Figure 5a shows the first plating and stripping half cycles for each of the three electrodes, with the circles labeled $t_1$ through $t_6$ corresponding to spectra shown in Fig. 5 and in Fig. S8 ($t_1$-$t_3$ are during deposition and $t_4$-$t_6$ are during stripping). The inset in Fig. 5a shows a magnified view of the end of the first stripping cycle, where alloy delithiation regions are evident. Figure 5b shows the total resistance $R_{tot}$ as a function of time for each type of electrode, with some of the individual spectra displayed in Fig. 5c-h. $R_{tot}$ is defined as the total width of each spectrum excluding the extended low-frequency tails of some plots, and $R_{tot}$ therefore accounts for both bulk SSE and interfacial resistance.

During the first stripping step from the bare Cu electrode (Fig. 5c), the observed spectra are quite similar, with only minor changes near the end of stripping ($t_6$, see Fig. 5b), suggesting retained contact at the interface. Note that the spectrum at $t_6$ is not the final spectrum after stripping (as was shown in Fig. 4), and therefore there is a lower interfacial resistance observed here than in Fig. 4. However, by the fifth stripping step of bare Cu (Fig. 5d), a larger high-frequency semicircular feature is present at the beginning of stripping. Over the course of stripping, this high-frequency feature expands, and another lower-frequency feature with apex frequency of ~150 Hz also arises. At $t_6$ near the end of stripping, these two features grow substantially but are still distinct. This lower-frequency feature is associated with constriction resistance due to contact loss near the end of stripping, as detailed subsequently. After polarizing completely at the end of stripping, these

two features merge, as previously shown in Fig. 4a; this merger could be due to changing interfacial geometry due to further contact loss.

To accompany these stripping data, Fig. S8a-b show spectral evolution during the first and fifth deposition half cycles for bare Cu corresponding to positions $t_1$ through $t_3$ in Fig. 5a. Like the stripping spectra, the spectra during the first deposition half-cycle remain similar. By the fifth cycle, however, the spectrum just after the onset of deposition ($t_1$) shows a low-frequency semicircle associated with contact loss that occurred at the end of the previous stripping half-cycle. Near the end of the deposition half-cycle ($t_3$), the width of the second semicircle has decreased, indicating contact re-establishment at the interface. The overall extracted resistance trends during these five cycles for bare Cu are shown in Fig. 5b; the total resistance of the bare Cu cell increases at the end of stripping and then decreases during subsequent plating, with a steadily increasing maximum $R_{tot}$ each cycle.

To verify that the observed EIS signatures primarily evolved due to contact loss and not due to other reasons such as the possible reactivity between Cu and LPSC, control experiments were carried out with two other types of working electrodes: bare stainless steel and 100 nm of Ni deposited on Cu foil (neither of which alloy with Li). Both types of working electrodes short circuited within a few cycles, similarly to Cu. The EIS spectra for stainless steel show the growth of a low-frequency semicircle near the end of stripping in the final cycle before short circuiting (Fig. S9). The Ni-coated Cu also shows a large low-frequency semicircle near the end of stripping (Fig. S10). Both sets of EIS signatures are similar to the bare Cu case, indicating that contact loss near the end of stripping drives this behavior for a variety of non-alloying electrodes with varying degrees of reactivity with LPSC.

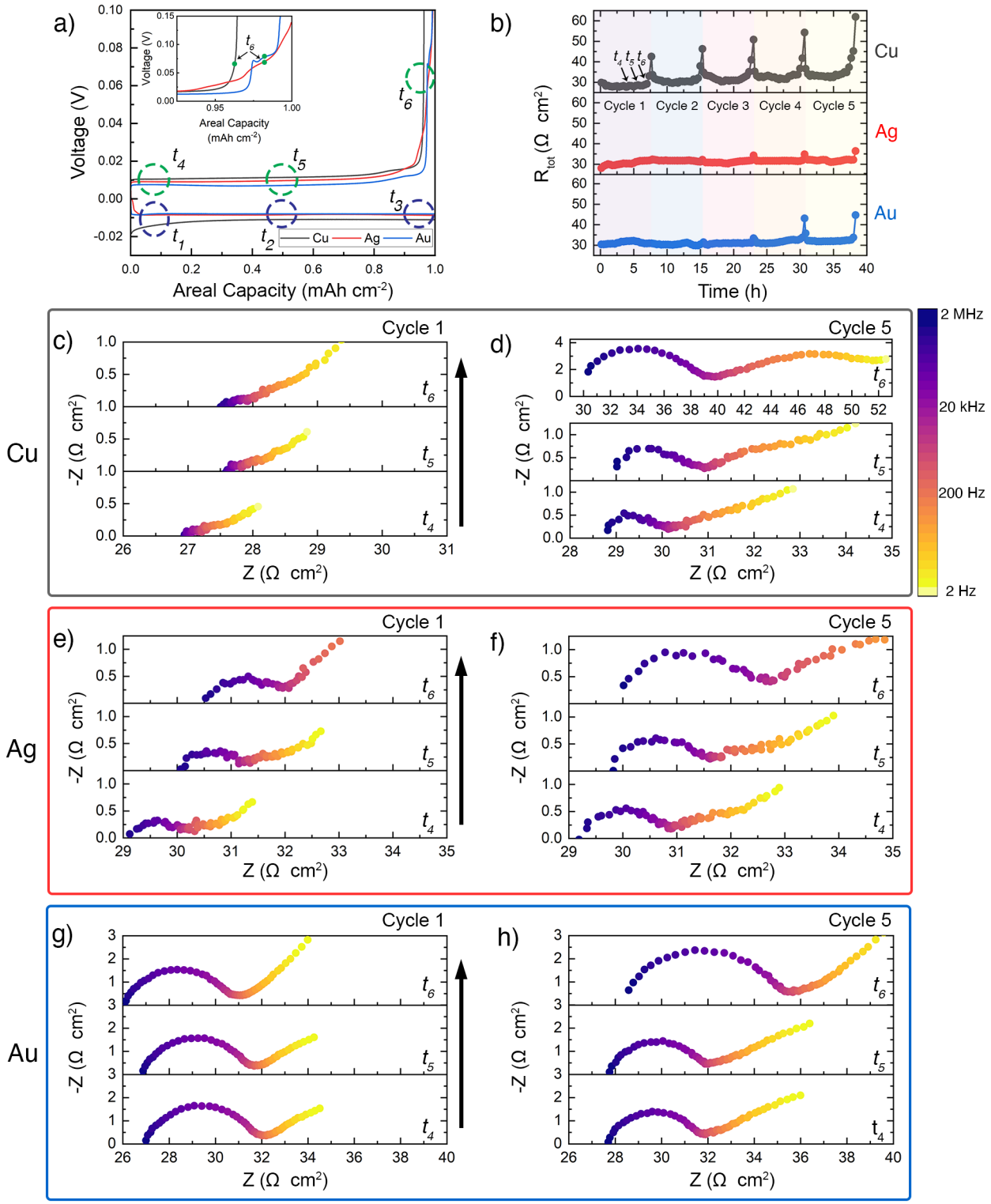


**Figure 5. *In situ* EIS analysis during Li plating/stripping.** (a) Typical first deposition/stripping curves for the three types of electrodes using a current density of 0.25 mA $cm^{-2}$ and areal capacity of 1.0 mAh $cm^{-2}$ (~5.0 μm of Li), with times $t_1$ through $t_6$ marked at which spectra are shown in this figure and in Fig. S8. The inset shows a magnified view of the curves near the end of stripping

with the EIS scans at $t_6$ indicated by green points. (b) Extracted total resistance $R_{tot}$ from the *in-situ* EIS analysis over five cycles for each type of cell, where $R_{tot}$ is defined as the total width of the spectra before the low-frequency tails of some plots. (c-d) Nyquist plots from a bare Cu half cell at times $t_4$ through $t_6$ during stripping during (c) the first cycle and (d) the fifth cycle. (e-f) Nyquist plots from a Ag-modified Cu half cell at times $t_4$ through $t_6$ during stripping during (e) the first cycle and (f) the fifth cycle. (g-h) Nyquist plots from a Au-modified Cu half cell at times $t_4$ through $t_6$ during stripping during (g) the first cycle and (h) the fifth cycle.

As recently discussed in detail,[31,59–62] contact loss at solid-state interfaces can cause complex evolution of EIS signatures. Contact loss causes constricted current pathways at the interface that can be described by 3D network models;[59] recent work has shown that conventional linear equivalent circuit models cannot effectively represent the influence of contact loss on EIS spectra.[60] The growth of the low-frequency feature near the end of stripping in Fig. 5d is likely associated with contact loss at the Cu working electrode, and indeed these spectra resemble other recent experimental work showing contact loss at $Li_6PS_5Cl$ interfaces.[61] The simultaneous growth of the higher-frequency semicircle (associated with interfacial impedance) in Fig. 5d is likely also influenced by contact loss. For these spectra, we do not attempt to use a linear equivalent circuit to ascribe individual features to distinct phenomena because of the convolution induced by the 3D nature of current flow at the interface due to contact loss. However, the increase of $R_{tot}$ at the end of each stripping step (Fig. 5b) is largely driven by increased constriction resistance and interfacial impedance.

The increased impedance driven by contact loss at the end of stripping of the bare Cu electrode in later cycles is direct evidence for the growth of voids at the working electrode interface. As we have recently described,[35] near the end of stripping, Li will be present across only part of the interface, as many regions will have been fully depleted of Li. The remaining pockets of Li still undergoing stripping will experience high local current densities and current constriction

effects because of the minimal electrochemically active interfacial area remaining. These high local current densities will exceed the current density necessary to form voids in certain locations,[26,34] and thus voids will form, as detected in the EIS spectra in Fig. 5d. This process is "intrinsic" in that it occurs due to the geometric depletion of Li even at low global current densities, in contrast to voiding which occurs across a uniform Li-excess interface when high current densities are applied.[26,35]

The Ag- and Au-modified electrodes exhibit distinct EIS evolution compared to the bare Cu case. During the first stripping half-cycle of the Ag-modified electrode (Fig. 5e), the electrode exhibits similar impedance spectra to that of bare Cu, but with a slightly larger semicircle (~1.5 Ω $cm^2$) denoting higher interfacial impedance. At the beginning of the fifth stripping cycle (Fig. 5f), the higher-frequency semicircle has grown slightly (~2 Ω $cm^2$) and expands to ~3 Ω $cm^2$ near the end of stripping. There is also a subtle elongation of the spectra at intermediate frequencies (~150 Hz), possibly associated with minor contact loss at the interface. During Li deposition on the Ag-modified electrodes (Fig. S8c), there is again little change in the spectral shapes in the first cycle. By the fifth cycle (Fig. S8d), the interfacial impedance at the onset of deposition is slightly larger and then decreases as contact is reestablished during deposition. We interpret these changes as evidence of some interfacial contact loss, but with much more substantial contact retained and thus lower total resistance than the bare Cu case (Fig. 5b shows the evolution of $R_{tot}$ across all five cycles for the Ag-modified electrode).

The Au-coated electrode (Fig. 5g) displays a larger high-frequency semicircle of about ~5 Ω $cm^2$ before any cycling and through the first deposition (Fig. S8e), which is retained without significant changes during the first stripping half-cycle (Fig. 5g). The larger semicircle indicates slightly higher interfacial impedance when using Au compared to Ag. During the fifth stripping

half-cycle (Fig. 5h), this high-frequency feature expands to ~8 Ω $cm^2$, without the obvious presence of lower-frequency features caused by contact loss. Thus, there is likely some contact rearrangement and current constriction with Au present, but again the interfacial impedance is much more stable than in the bare Cu case. Figure 5b shows the evolution of $R_{tot}$ for the Au-modified electrode, which shows slightly larger total resistance at the end of stripping than the Ag.

These EIS measurements show that Ag and Au alloy interlayers improve performance by largely mitigating voiding at the very end of stripping, which is the critical vulnerability of unmodified current collectors in anode-free cells. Although both the Au and Ag layers show extensive morphological evolution during Li growth (Fig. 2), thin layers of these materials still improve performance. From a morphological perspective, this is because both the Ag and Au materials return to the interface near the very end of stripping; the Au particles converge at the interface as the Li layer is removed, and the Ag precipitates from solution. Despite the morphological changes, these materials remain at the interface at the end of stripping and the beginning of deposition, which are the critical times for influencing electrochemical behavior.

**Governing Mechanisms and Electrochemical Modeling**

There are two possible reasons why these alloy interlayers act to improve interfacial contact retention. First, the alloy interlayers enable greater uniformity of Li deposition across the interfaces, as shown in Figs. 2-3. The alloy layers exhibit reduced nucleation overpotential (Fig. 1) and thus Li nuclei can continuously form at the interface,[44] resulting in dense Li layers with uniform thickness. Uniform Li layers are beneficial since they can be stripped to result in fewer regions of isolated Li remaining at the end of stripping, which exacerbates void formation.

The second possible effect could arise from the alloy layers responsively releasing Li via dealloying at local regions that experience increased current density near the end of stripping. To investigate this mechanism, we developed an electrochemical model that captures the electric potential response at the vicinity of an isolated Li island (see Experimental Procedures). Potential gradients can be influenced by the size of the Li island and ionic transport in the SSE, which in turn determine the overpotential ($\eta$) at the SSE/Li interface. The formation of an isolated Li island causes the surrounding Cu current collector to be directly interfaced with the SSE at the end of stripping, causing current constriction and void formation as the island shrinks (Fig. 6a). The presence of an alloy layer leads to the lithiated alloy around the Li island being interfaced with the SSE instead (Fig. 6b). This has an important mechanistic implication: when the overpotential at the SSE-alloy interface near the island becomes larger than the equilibrium potential for alloy delithiation, the alloy layer can start to delithiate during the stripping process (Fig. 6b), releasing Li where and when it is needed to homogenize the current distribution.

We modeled the electric potential response at isolated Li islands, and Fig. 6c shows a map of the overpotential at the SSE interface as a function of stripping current density and island size. These overpotentials are compared to the equilibrium potentials corresponding to the delithiation onset of Li-Ag (0.05 V vs. $Li/Li^+$) and Li-Au (0.07 V vs. $Li/Li^+$). The overpotential map in Fig. 6c features two dotted lines for the Li-Au and Li-Ag alloys, to the left of which the overpotential at the SSE interface is sufficiently high to locally delithiate the alloys and reduce current concentrations. The results show that the onset of alloy delithiation can be caused by sufficient shrinkage of the Li island or by an increase in the stripping current density. Figure 6d shows the potential distribution in the SSE ($\phi_{SSE}$) for a stripping current of 0.25 mA $cm^{-2}$ and an island size of 20 μm; the overpotential in this scenario (0.03 V) lies below the delithiation potential of the Li-

Ag and Li-Au alloys, implying that the alloys would not be delithiated. In contrast, for an island size of 5 μm, the constriction of ionic transport (Fig. 6e) results in an overpotential of 0.085 V, which would cause local delithiation of both alloys. For the electric potential distributions ($\phi_{SSE}$) shown in Fig. 6d, e, the Li island is present at the bottom boundary of the SE domain (Fig. S11). These results suggest that the proposed alloy-mediated mechanism could play an important role in mitigating current concentrations and void formation at the edge of small Li islands, which is of paramount importance in anode-free SSBs.

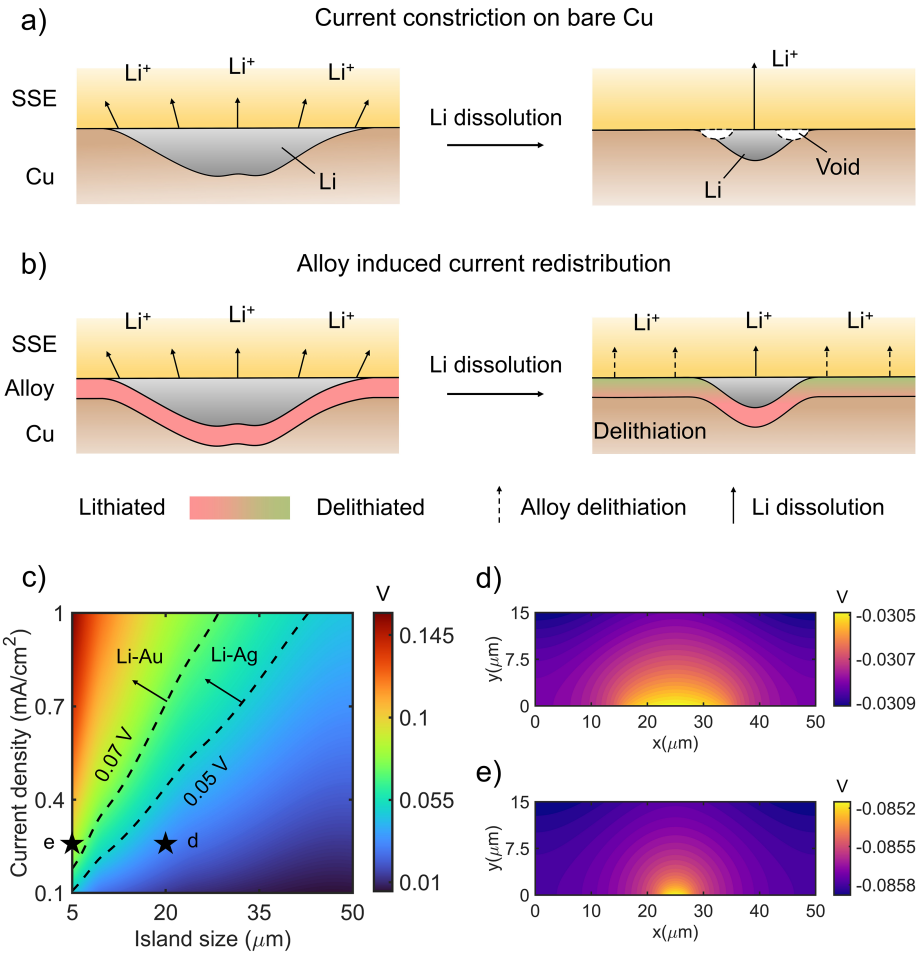


**Figure 6. Modeling of electric potential response at Li islands to evaluate the propensity for local delithiation of alloys**. This mechanism can homogenize reaction current and assist in mitigating void formation. (a) Illustration of stripping at an isolated Li island surrounded by the Cu current collector, which results in current constriction that causes void growth as the island shrinks. (b) Role of the alloy layer in regulating the current distribution. In response to the higher

overpotential due to current constriction at Li islands, the alloy layer delithiates and homogenizes current at the interface. Although the alloy layer is schematically shown beneath the Li, this does not have to be the case; even alloy materials distributed through the Li layer would return to the interface at the end of stripping. (c) Predicted overpotential ($\eta$) at the SSE surface as a function of the Li island size (i.e., Li domain size at the SSE interface) and stripping current density, along with dotted lines above which the Li-Ag and Li-Au alloys are expected to be delithiated. (d-e) Electric potential distribution in the SSE ($\phi_{SSE}$) for island sizes of (d) 20 μm and (e) 5 μm with a stripping current density of 0.25 mA cm$^{-2}$.

## CONCLUSIONS

This study advances our understanding of the role of alloy interlayers in improving performance of anode-free SSBs. Alloy interlayers show complex morphological evolution and influence multiple aspects of the electrochemical dynamics at the interface. Although the Ag and Au layers undergo different structural transformations during initial alloying and Li deposition (particle formation/breakup for Li-Au and dissolution for Li-Ag), they both improve Li nucleation density and thus allow for uniform Li growth across the current collector. Li with uniform thickness is less prone to islanding and void formation at the end of stripping, which enhances cycling stability. In addition, we show that alloy layers could serve to homogenize current in the vicinity of Li islands at the end of stripping due to localized delithiation driven by increased overpotential. This mechanism serves to further improve the resiliency and stability of these interfaces. A key feature of both the Au and Ag interlayers is that despite morphological evolution, they remain relatively uniformly dispersed after Li deposition (either as particles for Li-Au or dissolved for Li-Ag), enabling a return to the interface and consistent interfacial coverage upon Li removal. Other alloys with different reaction behavior, electrode potential, and/or mechanical properties may not meet this criterion. While both alloy layers significantly extended cyclability, we found evidence of agglomeration of the alloy materials with cycling that may influence the eventual failure via short circuiting. This agglomeration is likely accelerated by the uncontrolled

volume changes of the alloys, and future schemes to accommodate alloy transformation processes while homogeneously re-forming the alloy layer at the interface at the end of stripping (such as particle anchoring) would therefore be useful for further improving performance. Overall, the new understanding herein indicates that alloy layers hold significant promise toward enabling high-performance anode-free SSBs.

## EXPERIMENTAL PROCEDURES

### Resource availability

*Lead contact*

Further information and requests for resources and reagents should be directed to and will be fulfilled by the lead contact, Matthew McDowell (mattmcdowell@gatech.edu).

*Materials availability*

This study did not generate new unique reagents.

*Data and code availability*

All data associated with the study are included as supplementary data with this article.

**Material preparation.** $Li_6PS_5Cl$ powder (Ampcera) with particle size of ~10 μm was used for the SSE separator layer. 10-μm thick Cu foil (MTI) was used as the current collector and for deposition of alloy interlayers. 100 nm Ag, Au, or Ni interlayers were evaporated on a 10 μm thick

Cu foil in a CHA Mark 50 electron beam evaporator at a rate of 1 Å $s^{-1}$. Li metal foil (99.9% purity, MSE Supplies, Inc.) was cleaned and used as the counter electrode.

Single crystal $LiNi_{0.6}Mn_{0.2}Co_{0.2}O_2$ (NMC 622, MSE Supplies) was used as the active cathode material for full cell tests. To prevent side reactions with the $Li_6PS_5Cl$, the NMC particles were first coated with $LiNb_{0.5}Ta_{0.5}O_3$ (LNTO). LNTO was synthesized by mixing lithium acetate, niobium ethoxide, and tantalum butoxide in anhydrous ethanol (all from Sigma Aldrich) in a ratio of 20 mg lithium acetate, 36 µL niobium ethoxide, 60 µL tantalum butoxide, and 4 mL anhydrous ethanol for 6 h in an Ar-filled glove box (Vigor). The LNTO solution was then combined with NMC 622 in a ratio of 1 mL of LNTO solution to 2 g of NMC 622 and sonicated for 1 h to achieve a uniform dispersion. The solution was left in a vacuum oven at 80 °C overnight to remove the ethanol, leaving a dry mixture of NMC 622 with loosely coated LNTO. The mixture was then heat treated in a furnace by heating to 300 °C over 30 min, holding at 300 °C for 10 h, heating to 450 °C over 15 min, holding at 450 °C for 1 min, and then cooling the mixture to room temperature before removal. The composite cathodes were made with weight ratios of 70% LNTO-coated NMC-622, 27.5% ultrafine LPSC (MSE Supplies, particle size < 1 µm), and 2.5% vapor-grown carbon fibers (Sigma Aldrich). These components were milled into a composite using a Fritsch Pulverisette 7 ball mill in a zirconia jar with eight 10-mm zirconia balls. For the milling procedure, three cycles were performed with each cycle consisting of 10 min of milling at 150 RPM followed by 5 min of rest.

**Cell construction.** Anode-free half cells were constructed using custom cell housings that consist of a 10 mm PEEK die and two titanium rods, all within an Ar-filled glove box. Solid-state cell stacks were placed between two steel plates and a stack pressure was applied and controlled through the torque applied on the cell bolts.[51,58,63] 90 mg of LPSC was loaded into the PEEK die

and cold pressed between the two rods at 375 MPa for 1 min to form a pellet. 10 mm electrodes and ~0.3 mm Li were punched out and pressed onto either side of the LPSC pellet. Once fully assembled, the entire cell stack was then compressed at 15 MPa for 5 min to create contact at the solid-solid interface. Cells were loaded in between two steel plates and an applied stack pressure of 15 MPa was applied for operation.

**Electrochemical testing.** Electrochemical testing was conducted in an Ar-filled glove box using an Arbin battery cycler, with EIS measurements performed on a BioLogic SP-200 potentiostat. Cells were cycled at a current density of 0.25 mA $cm^{-2}$ with an areal capacity of 1.0 mAh $cm^{-2}$ unless otherwise specified. Voltage limits of - 0.5 V to 0.5 V and a half-cycle time cutoff of 4 h were used throughout cycling. EIS voltage limits were -1 V to 1 V. EIS measurements were performed with a frequency range of 2 MHz to 2 Hz. EIS spectra were collected every 10 min during deposition and stripping and at the end of each cycle. All experiments were conducted at room temperature (25 °C).

**SEM.** Electrodes were removed from cell stacks in an Ar-filled glove box and loaded onto an SEM stub and sample holder. The sample holder was sealed in an Ar-filled vial and then transferred into a vacuum-sealed box for transfer into the SEM. Upon loading the holder into the tool, samples were exposed to atmosphere for ~ 5 s. A Zeiss Ultra 50 field emission-SEM with an accelerating voltage of 5 kV and a working distance of ~9 mm was used to image these samples.

**Cryo-FIB.** Cryo-FIB/SEM experiments were performed on a Scios 2 Dual Beam SEM/FIB equipped with a Leica VCT cryogenic stage cooled to -145 °C. Samples were prepared in an Ar-filled glove box, coated with 7 nm of Pt using a cryo-sputter coater (ACE 600), and transferred to the cryo-FIB/SEM under high vacuum using the Leica VCT500 shuttle. Secondary electron imaging was performed at 5 keV/50 pA and $Ga^+$ ion FIB milling was performed with an

accelerating voltage of 16 keV. X-ray energy dispersive spectroscopy (EDS) maps were collected using an EDAX Octane Elite detector.

**Plasma FIB.** Plasma-FIB characterization was carried out on a Helios G4 PFIB UXE equipped with a $Xe^+$ ion source. Samples were rapidly transferred to the vacuum chamber with minimal air exposure (<15 s). Trenches were milled at an accelerating voltage of 30 kV and an ion beam current of 500 nA. Final cleaning cuts were milled at 30 kV and 60 nA. . Secondary electron images were recorded at both 2 and 20 kV. EDS data were collected at 20 kV for qualitative chemical species mapping using an EDAX Octane Elite spectrometer.

**X-ray micro CT.** X-ray μCT scans of anode-free SSBs were collected at the Advanced Photon Source using beamline 2-BM. Monochromatic X-rays with an energy of 25.5 keV were used. 1500 projections were collected over an angle of 180° with an exposure time of 400 ms per image using an optics system consisting of an Oryx 5.0 MP Mono 10GigE detector and a 2× magnification lens. The voxel size was 1.7 μm. A specialized cell housing with cell diameter of 2 mm was used to image these cells, as used in previous studies.[35,64] 6 mg of ground LPSC was pelletized within the polyether ether ketone (PEEK) cell housing at 225 MPa. A 2 mm disk of Li foil as the counter electrode and either bare Cu foil or Ag-coated Cu foil as the working electrode was inserted. Screws were used to seal and tighten the cell to a stack pressure of ~10 MPa. 2 mAh $cm^{-2}$ of Li was deposited using a current density of 0.5 mA $cm^{-2}$ on both bare Cu and Ag-coated Cu to ensure the Li was thick enough for imaging in the limited time available for the experiment. Raw data was reconstructed with TomoPy via the GridRec method. Image segmentation/analysis and 3D rendering creation were performed using DragonFly with some processing done through MATBOX.[65] Segmented phases were then processed in MATLAB to analyze the thickness variations across interfaces.

**Electrochemical modeling.** The electric potential distribution in the SSE domain was described using the following governing equation:

$$\nabla.(k_{SSE}\,\nabla\phi_{SSE}) = 0$$

Here, $k_{SSE}$ is the ionic conductivity of the SSE and $\phi_{SSE}$ is the electric potential in response to ionic transport in the SE. Based on the materials used in this work, $k_{SSE}$ is taken as $1.8 \times 10^{-3}$ S/cm[58]. The dimensions of the SSE domain, as shown in Fig. 6d, e, are 50 μm × 15 μm. The current density ($I_{app}$) is applied at the top boundary of the SSE: $-k_{SSE}\,\nabla\phi_{SSE} = I_{app}$. At the left and right boundaries $\nabla\phi_{SSE}.n = 0$. The presence of the Li island is considered at the bottom boundary of the SSE (see Fig. S11). For the SSE/Li interface at the bottom boundary of the domain, the electrochemical reactions are captured using the Butler–Volmer expression: $-k_{SSE}\nabla\phi_{SSE} = i_0\left(exp\left(\frac{\alpha_a F}{RT}\eta\right) - exp\left(-\frac{\alpha_c F}{RT}\eta\right)\right)$. Here, $F$ is the Faraday constant, $R$ is the gas constant, $i_0$ is the exchange current density, $T$ is the temperature, $\alpha_a$ and $\alpha_c$ are the charge transfer coefficients, and $\eta$ is the overpotential. At regions at the bottom SSE boundary that are not in contact with Li, $\nabla\phi_{SE}.n = 0$. The computational domain is shown in Fig. S11.

## ACKNOWLEDGMENTS

This work was supported by the Center for Mechano-Chemical Understanding of Solid Ion Conductors (MUSIC), an Energy Frontier Research Center funded by the U.S. Department of Energy, Office of Science, Office of Basic Energy Sciences under contract DE-SC0023438. A portion of this work was performed at the Center for Integrated Nanotechnologies, an Office of Science User Facility operated for the U.S. Department of Energy, Office of Science. Los Alamos National Laboratory, an affirmative action equal opportunity employer, is managed by Triad National Security, LLC for the U.S. Department of Energy's NNSA, under contract

89233218CNA000001. This research additionally used resources of the Advanced Photon Source, a U.S. Department of Energy (DOE) Office of Science user facility operated for the DOE Office of Science by Argonne National Laboratory under Contract No. DE-AC02-06CH11357. S.E.S acknowledges support from an NSF Graduate Research Fellowship under grant no. DGE-1650044, U.S Department of Energy Office of Science Graduate Student Research (SCGSR) program under contract no. DE-SC0014664, and a Sloan Foundation MPHD Program Scholarship.

AUTHOR CONTRIBUTIONS

**Stephanie Elizabeth Sandoval** conceptualization, methodology, validation, formal analysis, investigation, writing – original draft, writing – review & editing, visualization, funding acquisition; **John A. Lewis** investigation; **Bairav S. Vishnugopi** software, formal analysis; **Douglas Lars Nelson** investigation; **Matthew M. Schneider** investigation, resources; **Francisco Javier Quintero Cortes** formal analysis; **Christopher M. Matthews** resources, visualization; **John Watt** resources; **Mengkun Tian** resources; **Pavel Shevchenko** investigation; **Partha P. Mukherjee** formal analysis; **Matthew T. McDowell** conceptualization, methodology, supervision, writing-original draft, writing-review & editing, supervision, funding acquisition.

## DECLARATION OF INTERESTS

The authors declare no competing interests.

REFERENCES


1. Famprikis, T., Canepa, P., Dawson, J.A., Islam, M.S., and Masquelier, C. (2019). Fundamentals of inorganic solid-state electrolytes for batteries. Nat. Mater. *18*, 1278–1291. 10.1038/s41563-019-0431-3.

2. Janek, J., and Zeier, W.G. (2016). A solid future for battery development. Nat. Energy *1*, 16141. 10.1038/nenergy.2016.141.

3. Manthiram, A., Yu, X., and Wang, S. (2017). Lithium battery chemistries enabled by solid-state electrolytes. Nat. Rev. Mater. *2*, 16103. 10.1038/natrevmats.2016.103.

4. Shen, Y., Zhang, Y., Han, S., Wang, J., Peng, Z., and Chen, L. (2018). Unlocking the energy capabilities of lithium metal electrode with solid-state electrolytes. Joule *2*, 1674–1689. 10.1016/j.joule.2018.06.021.

5. Hatzell, K.B., Chen, X.C., Cobb, C.L., Dasgupta, N.P., Dixit, M.B., Marbella, L.E., McDowell, M.T., Mukherjee, P.P., Verma, A., Viswanathan, V., et al. (2020). Challenges in lithium metal anodes for solid-state batteries. ACS Energy Lett. *5*, 922–934. 10.1021/acsenergylett.9b02668.

6. Vishnugopi, B.S., Kazyak, E., Lewis, J.A., Nanda, J., McDowell, M.T., Dasgupta, N.P., and Mukherjee, P.P. (2021). Challenges and opportunities for fast charging of solid-state lithium metal batteries. ACS Energy Lett. *6*, 3734–3749.

7. McDowell, M.T., Quintero Cortes, F.J., Thenuwara, A.C., and Lewis, J.A. (2020). Toward high-capacity battery anode materials: chemistry and mechanics intertwined. Chem. Mater. *32*, 8755–8771. 10.1021/acs.chemmater.0c02981.

8. Heubner, C., Maletti, S., Auer, H., Hüttl, J., Voigt, K., Lohrberg, O., Nikolowski, K., Partsch, M., and Michaelis, A. (2021). From lithium-metal toward anode-free solid-state

batteries: current developments, issues, and challenges. Adv. Funct. Mater. *31*, 2106608. 10.1002/adfm.202106608.

9. Wang, M.J., Carmona, E., Gupta, A., Albertus, P., and Sakamoto, J. (2020). Enabling "lithium-free" manufacturing of pure lithium metal solid-state batteries through in situ plating. Nat. Commun. *11*, 5201. 10.1038/s41467-020-19004-4.

10. Qian, J., Adams, B.D., Zheng, J., Xu, W., Henderson, W.A., Wang, J., Bowden, M.E., Xu, S., Hu, J., and Zhang, J.G. (2016). Anode-free rechargeable lithium metal batteries. Adv. Funct. Mater. *26*, 7094–7102. 10.1002/adfm.201602353.

11. Louli, A.J., Eldesoky, A., Weber, R., Genovese, M., Coon, M., deGooyer, J., Deng, Z., White, R.T., Lee, J., Rodgers, T., et al. (2020). Diagnosing and correcting anode-free cell failure via electrolyte and morphological analysis. Nat. Energy *5*, 693–702. 10.1038/s41560-020-0668-8.

12. Lee, Y.G., Fujiki, S., Jung, C., Suzuki, N., Yashiro, N., Omoda, R., Ko, D.S., Shiratsuchi, T., Sugimoto, T., Ryu, S., et al. (2020). High-energy long-cycling all-solid-state lithium metal batteries enabled by silver–carbon composite anodes. Nat. Energy *5*, 299–308. 10.1038/s41560-020-0575-z.

13. Xie, Z., Wu, Z., An, X., Yue, X., Wang, J., Abudula, A., and Guan, G. (2020). Anode-free rechargeable lithium metal batteries: progress and prospects. Energy Storage Mater. *32*, 386–401. 10.1016/j.ensm.2020.07.004.

14. Tong, Z., Bazri, B., Hu, S.F., and Liu, R.S. (2021). Interfacial chemistry in anode-free batteries: challenges and strategies. J. Mater. Chem. A *9*, 7396–7406. 10.1039/d1ta00419k.

15. Nanda, S., Gupta, A., and Manthiram, A. (2021). Anode-free full cells: a pathway to high-

energy density lithium-metal batteries. Adv. Energy Mater. *11*, 2000804. 10.1002/aenm.202000804.

16. Huang, C.J., Thirumalraj, B., Tao, H.C., Shitaw, K.N., Sutiono, H., Hagos, T.T., Beyene, T.T., Kuo, L.M., Wang, C.C., Wu, S.H., et al. (2021). Decoupling the origins of irreversible coulombic efficiency in anode-free lithium metal batteries. Nat. Commun. *12*, 1452. 10.1038/s41467-021-21683-6.

17. Krauskopf, T., Richter, F.H., Zeier, W.G., and Janek, J. (2020). Physicochemical concepts of the lithium metal anode in solid-state batteries. Chem. Rev. *120*, 7745–7794. 10.1021/acs.chemrev.0c00431.

18. Wenzel, S., Weber, D.A., Leichtweiss, T., Busche, M.R., Sann, J., and Janek, J. (2016). Interphase formation and degradation of charge transfer kinetics between a lithium metal anode and highly crystalline $Li_7P_3S_{11}$ solid electrolyte. Solid State Ionics *286*, 24–33. 10.1016/j.ssi.2015.11.034.

19. Richards, W.D., Miara, L.J., Wang, Y., Kim, J.C., and Ceder, G. (2016). Interface stability in solid-state batteries. Chem. Mater. *28*, 266–273. 10.1021/acs.chemmater.5b04082.

20. Han, X., Gong, Y., Fu, K., He, X., Hitz, G.T., Dai, J., Pearse, A., Liu, B., Wang, H., Rubloff, G., et al. (2017). Negating interfacial impedance in garnet-based solid-state Li metal batteries. Nat. Mater. *16*, 572–579. 10.1038/nmat4821.

21. Kasemchainan, J., Zekoll, S., Spencer Jolly, D., Ning, Z., Hartley, G.O., Marrow, J., and Bruce, P.G. (2019). Critical stripping current leads to dendrite formation on plating in lithium anode solid electrolyte cells. Nat. Mater. *18*, 1105–1111. 10.1038/s41563-019-0438-9.

22. Sandoval, S.E., Cortes, F.J.Q., Klein, E.J., Lewis, J.A., Shetty, P.P., Yeh, D., and

McDowell, M.T. (2021). Understanding the effects of alloy films on the electrochemical behavior of lithium metal anodes with operando optical microscopy. J. Electrochem. Soc. *168*, 100517. 10.1149/1945-7111/ac2d11.

23. Koerver, R., Zhang, W., De Biasi, L., Schweidler, S., Kondrakov, A.O., Kolling, S., Brezesinski, T., Hartmann, P., Zeier, W.G., and Janek, J. (2018). Chemo-mechanical expansion of lithium electrode materials-on the route to mechanically optimized all-solid-state batteries. Energy Environ. Sci. *11*, 2142–2158. 10.1039/c8ee00907d.

24. Vishnugopi, B.S., Naik, K.G., Kawakami, H., Ikeda, N., Mizuno, Y., Iwamura, R., Kotaka, T., Aotani, K., Tabuchi, Y., and Mukherjee, P.P. (2022). Asymmetric contact loss dynamics during plating and stripping in solid-state batteries. Adv. Energy Mater., 2203671. 10.1002/aenm.202203671.

25. Wang, M.J., Choudhury, R., and Sakamoto, J. (2019). Characterizing the Li-solid-electrolyte interface dynamics as a function of stack pressure and current density. Joule *3*, 2165–2178. 10.1016/j.joule.2019.06.017.

26. Kasemchainan, J., Zekoll, S., Spencer Jolly, D., Ning, Z., Hartley, G.O., Marrow, J., and Bruce, P.G. (2019). Critical stripping current leads to dendrite formation on plating in lithium anode solid electrolyte cells. Nat. Mater. *18*, 1105–1111. 10.1038/s41563-019-0438-9.

27. Porz, L., Swamy, T., Sheldon, B.W., Rettenwander, D., Frömling, T., Thaman, H.L., Berendts, S., Uecker, R., Carter, W.C., and Chiang, Y.M. (2017). Mechanism of lithium metal penetration through inorganic solid electrolytes. Adv. Energy Mater. *7*, 1701003. 10.1002/aenm.201701003.

28. Kazyak, E., Garcia-Mendez, R., LePage, W.S., Sharafi, A., Davis, A.L., Sanchez, A.J.,

Chen, K.H., Haslam, C., Sakamoto, J., and Dasgupta, N.P. (2020). Li penetration in ceramic solid electrolytes: operando microscopy analysis of morphology, propagation, and reversibility. Matter *2*, 1025–1048. 10.1016/j.matt.2020.02.008.

29. Liu, J., Bao, Z., Cui, Y., Dufek, E.J., Goodenough, J.B., Khalifah, P., Li, Q., Liaw, B.Y., Liu, P., Manthiram, A., et al. (2019). Pathways for practical high-energy long cycling lithium metal batteries. Nat. Energy *4*, 180–186. 10.1038/s41560-019-0338-x.

30. Wolfenstine, J., Allen, J.L., Sakamoto, J., Siegel, D.J., and Choe, H. (2018). Mechanical behavior of Li-ion-conducting crystalline oxide-based solid electrolytes: a brief review. Ionics *24*, 1271–1276. 10.1007/s11581-017-2314-4.

31. Krauskopf, T., Hartmann, H., Zeier, W.G., and Janek, J. (2019). Toward a fundamental understanding of the lithium metal anode in solid-state batteries - an electrochemo-mechanical study on the garnet-type solid electrolyte $Li_{6.25}Al_{0.25}La_3Zr_2O_{12}$. ACS Appl. Mater. Interfaces *11*, 14463–14477. 10.1021/acsami.9b02537.

32. Krauskopf, T., Dippel, R., Hartmann, H., Peppler, K., Mogwitz, B., Richter, F.H., Zeier, W.G., and Janek, J. (2019). Lithium-metal growth kinetics on LLZO garnet-type solid electrolytes. Joule *3*, 2030–2049. 10.1016/j.joule.2019.06.013.

33. Kazyak, E., Wang, M.J., Lee, K., Yadavalli, S., Sanchez, A.J., Thouless, M.D., Sakamoto, J., and Dasgupta, N.P. (2022). Understanding the electro-chemo-mechanics of Li plating in anode-free solid-state batteries with operando 3D microscopy. Matter *5*, 3912–3934. 10.1016/j.matt.2022.07.020.

34. Lee, K., Kazyak, E., Wang, M.J., Neil, P., and Sakamoto, J. (2022). Analyzing void formation and rewetting of thin in situ-formed Li anodes on LLZO. Joule *6*, 2547–2565. 10.1016/j.joule.2022.09.009.

35. Lewis, J.A., Sandoval, S.E., Liu, Y., Nelson, D.L., Yoon, S.G., Wang, R., Zhao, Y., Tian, M., Shevchenko, P., Martínez-Pañeda, E., et al. (2023). Accelerated short circuiting in anode-free solid-state batteries driven by local lithium depletion. Adv. Energy Mater. *2204186*, 1–12. 10.1002/aenm.202204186.

36. Liu, M., Wang, C., Cheng, Z., Ganapathy, S., Haverkate, L.A., Unnikrishnan, S., and Wagemaker, M. (2020). Controlling the Li-metal growth to enable low Li-metal excess all solid state Li-metal batteries. ACS Mater. Lett. *2*, 665–670. 10.1021/acsmaterialslett.0c00152.

37. Yang, C., Xie, H., Ping, W., Fu, K., Liu, B., Rao, J., Dai, J., Wang, C., Pastel, G., and Hu, L. (2019). An electron/ion dual-conductive alloy framework for high-rate and high-capacity solid-state lithium-metalbatteries. Adv. Mater. *31*, 1804815. 10.1002/adma.201804815.

38. Wang, Y., Liu, Y., Nguyen, M., Cho, J., Katyal, N., Bairav, S., Hao, H., Fang, R., Wu, N., Liu, P., et al. (2022). Stable anode-free all-solid-state lithium battery through tuned metal wetting on the copper current collector. Adv. Mater., 2206762. 10.1002/adma.202206762.

39. Hiratani, M., Miyauchi, K., and Kudo, T. (1988). Effect of a lithium alloy layer inserted between a lithium anode and a solid electrolyte. Solid State Ionics *28–30*, 1406–1410. 10.1016/0167-2738(88)90394-3.

40. Cho, S., Kim, D.Y., Lee, J.I., Kang, J., Lee, H., Kim, G., Seo, D.H., and Park, S. (2022). Highly reversible lithium host materials for high-energy-density anode-free lithium metal batteries. Adv. Funct. Mater. *32*. 10.1002/adfm.202208629.

41. Haslam, C., and Sakamoto, J. (2023). Stable Lithium Plating in " Lithium Metal-Free " Solid-State Batteries Enabled by Seeded Lithium Nucleation. J. Electrochem. Soc. *170*.

10.1149/1945-7111/accab4.

42. Krauskopf, T., Mogwitz, B., Rosenbach, C., Zeier, W.G., and Janek, J. (2019). Diffusion limitation of lithium metal and Li–Mg alloy anodes on LLZO type solid electrolytes as a function of temperature and pressure. Adv. Energy Mater. *9*, 1902568. 10.1002/aenm.201902568.

43. Guan, X., Wang, A., Liu, S., Li, G., Liang, F., Yang, Y.W., Liu, X., and Luo, J. (2018). Controlling nucleation in lithium metal anodes. Small *14*, 1801423. 10.1002/smll.201801423.

44. Pei, A., Zheng, G., Shi, F., Li, Y., and Cui, Y. (2017). Nanoscale nucleation and growth of electrodeposited lithium metal. Nano Lett. *17*, 1132–1139. 10.1021/acs.nanolett.6b04755.

45. Biswal, P., Stalin, S., Kludze, A., Choudhury, S., and Archer, L.A. (2019). Nucleation and early stage growth of Li electrodeposits. Nano Lett. *19*, 8191–8200. 10.1021/acs.nanolett.9b03548.

46. Yan, K., Lu, Z., Lee, H.W., Xiong, F., Hsu, P.C., Li, Y., Zhao, J., Chu, S., and Cui, Y. (2016). Selective deposition and stable encapsulation of lithium through heterogeneous seeded growth. Nat. Energy *1*, 16010. 10.1038/nenergy.2016.10.

47. Tan, D.H.S., Banerjee, A., Chen, Z., and Meng, Y.S. (2020). From nanoscale interface characterization to sustainable energy storage using all-solid-state batteries. Nat. Nanotechnol. *15*, 170–180. 10.1038/s41565-020-0657-x.

48. Zhang, M., Chouchane, M., Shojaee, S.A., Winiarski, B., Liu, Z., Li, L., Pelapur, R., Shodiev, A., Yao, W., Doux, J.-M., et al. (2022). Coupling of multiscale imaging analysis and computational modeling for understanding thick cathode degradation mechanisms. Joule *7*, 201-220. 10.1016/j.joule.2022.12.001.

49. Lee, J.Z., Wynn, T.A., Schroeder, M.A., Alvarado, J., Wang, X., Xu, K., and Meng, Y.S. (2019). Cryogenic focused ion beam characterization of lithium metal anodes. ACS Energy Lett. *4*, 489–493. 10.1021/acsenergylett.8b02381.

50. Cheng, D., Lu, B., Raghavendran, G., Zhang, M., and Meng, Y.S. (2022). Leveraging cryogenic electron microscopy for advancing battery design. Matter *5*, 26–42. 10.1016/j.matt.2021.11.019.

51. Han, S.Y., Lee, C., Lewis, J.A., Yeh, D., Liu, Y., Lee, H.W., and McDowell, M.T. (2021). Stress evolution during cycling of alloy-anode solid-state batteries. Joule *5*, 2450–2465. 10.1016/j.joule.2021.07.002.

52. Jin, S., Ye, Y., Niu, Y., Xu, Y., Jin, H., Wang, J., Sun, Z., Cao, A., Wu, X., Luo, Y., et al. (2020). Solid–solution-based metal alloy phase for highly reversible lithium metal anode. J. Am. Chem. Soc. *142*, 8818–8826. 10.1021/jacs.0c01811.

53. Pelton, A.D. (1986). The Ag−Li (silver-lithium) system. Bull. Alloy Phase Diagrams *7*, 223–228. 10.1007/bf02868993.

54. Yang, C., Yao, Y., He, S., Xie, H., Hitz, E., and Hu, L. (2017). Ultrafine silver nanoparticles for seeded lithium deposition toward stable lithium metal anode. Adv. Mater. *29*, 1–8. 10.1002/adma.201702714.

55. Pelton, A.D. (1986). The Au-Li (gold-lithium) system. Bull. Alloy Phase Diagrams *7*, 228–231. 10.1007/BF02868994.

56. Ohno, S., Bernges, T., Buchheim, J., Duchardt, M., Hatz, A.K., Kraft, M.A., Kwak, H., Santhosha, A.L., Liu, Z., Minafra, N., et al. (2020). How certain are the reported ionic conductivities of thiophosphate-based solid electrolytes? An interlaboratory study. ACS Energy Lett. *5*, 910–915. 10.1021/acsenergylett.9b02764.

57. Kraft, M.A., Culver, S.P., Calderon, M., Böcher, F., Krauskopf, T., Senyshyn, A., Dietrich, C., Zevalkink, A., Janek, J., and Zeier, W.G. (2017). Influence of lattice polarizability on the ionic conductivity in the lithium superionic argyrodites $Li_6PS_5X$ (X = Cl, Br, I). J. Am. Chem. Soc. *139*, 10909–10918. 10.1021/jacs.7b06327.

58. Lee, C., Han, S.Y., Lewis, J.A., Shetty, P.P., Yeh, D., Liu, Y., Klein, E., Lee, H.W., and McDowell, M.T. (2021). Stack pressure measurements to probe the evolution of the lithium-solid-state electrolyte interface. ACS Energy Lett. *6*, 3261–3269. 10.1021/acsenergylett.1c01395.

59. Eckhardt, J.K., Klar, P.J., Janek, J., and Heiliger, C. (2022). Interplay of dynamic constriction and interface morphology between reversible metal anode and solid electrolyte in solid state batteries. ACS Appl. Mater. Interfaces *14*, 35545–35554. 10.1021/acsami.2c07077.

60. Eckhardt, J.K., Fuchs, T., Burkhardt, S., Klar, P.J., Janek, J., and Heiliger, C. (2022). 3D impedance modeling of metal anodes in solid-state batteries-incompatibility of pore formation and constriction effect in physical-based 1D circuit models. ACS Appl. Mater. Interfaces *14*, 42757–42769. 10.1021/acsami.2c12991.

61. Singh, D.K., Henss, A., Mogwitz, B., Gautam, A., Horn, J., Krauskopf, T., Burkhardt, S., Sann, J., Richter, F.H., and Janek, J. (2022). $Li_6PS_5Cl$ microstructure and influence on dendrite growth in solid-state batteries with lithium metal anode. Cell Reports Phys. Sci. *3*, 101043. 10.1016/j.xcrp.2022.101043.

62. Krauskopf, T., Mogwitz, B., Hartmann, H., Singh, D.K., Zeier, W.G., and Janek, J. (2020). The fast charge transfer kinetics of the lithium metal anode on the garnet-type solid electrolyte $Li_{6.25}Al_{0.25}La_3Zr_2O_{12}$. Adv. Energy Mater. *10*, 2000945.

10.1002/aenm.202000945.

63. Lewis, J.A., Lee, C., Liu, Y., Han, S.Y., Prakash, D., Klein, E.J., Lee, H.W., and McDowell, M.T. (2022). Role of areal capacity in determining short circuiting of sulfide-based solid-state batteries. ACS Appl. Mater. Interfaces *14*, 4051–4060. 10.1021/acsami.1c20139.

64. Lewis, J.A., Cortes, F.J.Q., Liu, Y., Miers, J.C., Verma, A., Vishnugopi, B.S., Tippens, J., Prakash, D., Marchese, T.S., Han, S.Y., et al. (2021). Linking void and interphase evolution to electrochemistry in solid-state batteries using operando X-ray tomography. Nat. Mater. *20*, 503–510. 10.1038/s41563-020-00903-2.

65. Usseglio-Viretta, F.L.E., Patel, P., Bernhardt, E., Mistry, A., Mukherjee, P.P., Allen, J., Cooper, S.J., Laurencin, J., and Smith, K. (2022). MATBOX: An Open-source Microstructure Analysis Toolbox for microstructure generation, segmentation, characterization, visualization, correlation, and meshing. SoftwareX *17*, 100915. 10.1016/j.softx.2021.100915.